Precision Optimization and Path Planning of Industrial Robots Based on Force-Position Cooperative Control in Incremental Metal Forming

Siwen Liu[1*]

[1] Guangdong Beyho Technology Co.,LTD. , Foshan, 528000, China

* 385284030@qq.com

https://doi.org/10.70695/IAAI202504A11

Abstract

Industrial robots face challenges in incremental forming, including insufficient precision, significant force fluctuations, and a lack of closed-loop path planning. To address these issues, this study presents an integrated approach combining force-position co-control with error-driven path improvement. First, a dynamic model is created, incorporating contact stiffness and elastic recovery to represent the coupling relationship between end-effector pose and forming force. Then, a discrete observer is formed based on the observability of the error, enabling real-time estimation of nodal normal errors. The estimation results are combined with piecewise segmentation of the forming force gradient and refinement of the error field to obtain an adaptive path planning framework. Experiments on a six-axis robot platform demonstrate that this method reduces the mean square error of the trajectory by approximately 40%, normal force fluctuation by approximately 35%, and contour error in high-curvature regions by approximately 45%. Furthermore, it maintains stable generalization performance under various material and plate thickness conditions, providing a feasible technical approach for high-precision and robust control of robot incremental forming.

Keywords Industrial Robot; Incremental Metal Forming; Force-position Cooperative Control; Error Observation; Path Planning Optimization

1 Introduction

The impact of force fluctuations and path deviations caused by contact nonlinearity in robot incremental forming on accuracy is significant. Čabaravdić et al. showed that position control is difficult to suppress the instability of force, so they proposed force control path planning [1]. Johra et al. used elastic-geometric models and force feedback to achieve instant compensation, but it was still affected by elastic recovery [2]. Kang et al. used the stiffness ellipsoid method to improve the cooperative control under high stiffness conditions [3]. Ye et al. gave a hybrid position-moment compensation strategy, but it is still sensitive to dynamic disturbances [4]. To et al. further introduced a deep neural network compensator to achieve joint optimization of trajectory and moment compensation [5]. In terms of collaborative and compliant control, Li et al. proposed hierarchical constraints [6]. Han et al. possessed active compliance capability [7]. Liu et al. realized variable load force control [8], all of which demonstrate the significant impact of disturbance on accuracy. In terms of forming path design, Bârsan et al. systematically analyzed the significant impact of path strategy on local quality [9]. Racz et al. connected trajectory planning with dynamic estimation, emphasizing the importance of dynamic adaptation for stable forming [10]. Overall, existing methods still have shortcomings in the collaboration between force control and path planning and online closed-loop compensation. Based on this, this study proposes a highly coupled force-position collaboration and error-driven path improvement framework to improve the accuracy and stability of robot incremental forming.

2 Modeling and Structural Design of Force-Position Coordinated Control System

2.1 Dynamic Modeling of Industrial Robots in Incremental Molding

During the incremental prototyping process of a robot, the manipulator needs to maintain stable trajectory tracking under conditions of significant external loads and contact disturbances. To address this, a rigid body dynamics model is first established in joint space, and an end-effector contact force term is explicitly introduced as a unified basis for subsequent force-position coordinated control and simulation.

$$\mathbf{M}(\mathbf{q})\ddot{\mathbf{q}}+\mathbf{C}(\mathbf{q},\dot{\mathbf{q}})\dot{\mathbf{q}}+\mathbf{G}(\mathbf{q})=\boldsymbol{\tau}+\mathbf{J}\ \ (\mathbf{q})\mathbf{F}_e \tag{1}$$

Where $\mathbf{q}$ represents the joint angle vector, $\ddot{\mathbf{q}}$ represents the joint angular acceleration, $\mathbf{M}(\mathbf{q})$ is the mass matrix, $\mathbf{C}(\mathbf{q},\dot{\mathbf{q}})$ is the Coriolis and eccentric term matrix, $\mathbf{G}(\mathbf{q})$ is the gravity vector, $\boldsymbol{\tau}$ is the joint driving torque, $\mathbf{J}(\mathbf{q})$ is the Jacobian matrix, $\mathbf{F}_e$ and is the end contact force vector.

To maintain consistency with the task space path planning, a mapping relationship between joints and end effector motion needs to be established:

$$\dot{\mathbf{x}}=\mathbf{J}(\mathbf{q})\dot{\mathbf{q}},\quad \ddot{\mathbf{x}}=\mathbf{J}(\mathbf{q})\ddot{\mathbf{q}}+\dot{\mathbf{J}}(\mathbf{q})\dot{\mathbf{q}} \tag{2}$$

In the formula, $\mathbf{x}$ represents the end-effector pose vector, which contains position and attitude information; $\dot{\mathbf{x}}$ represents the end-effector velocity vector; $\ddot{\mathbf{x}}$ represents the end-effector acceleration vector; $\ddot{\mathbf{q}}$ is the joint angular velocity vector; $\dot{\mathbf{J}}(\mathbf{q})$ is the derivative of the Jacobian matrix with respect to time, and other symbols are the same as in formula (1).

In the control implementation, inverse dynamics can be used to generate feedforward torque to compensate for the body's inertia and gravity:

$$\boldsymbol{\tau}=\mathbf{M}(\mathbf{q})\mathbf{J}^{-1}(\mathbf{q})(\ddot{\mathbf{x}}-\dot{\mathbf{J}}(\mathbf{q})\dot{\mathbf{q}})+\mathbf{C}(\mathbf{q},\dot{\mathbf{q}})\dot{\mathbf{q}}+\mathbf{G}(\mathbf{q}) \tag{3}$$

In the formula, $\mathbf{J}^{-1}(\mathbf{q})$ is the inverse or generalized inverse of the Jacobian matrix; $\ddot{\mathbf{x}}$ is the desired terminal acceleration vector; the other symbols are consistent with the meanings of equations (1) and (2).

2.2 Coupling Mechanism between End Deformation and Contact Force

In incremental forming, the local contact stiffness between the tool tip and the sheet metal determines the forming force level and its fluctuation characteristics. To describe the coupling relationship between end displacement and contact force, an equivalent linear stiffness model is used at the tool-sheet interface, corresponding to normal indentation and tangential slip as contact force components:

$$\mathbf{F}_e=\begin{bmatrix}F_n\\F_t\end{bmatrix}=\begin{bmatrix}k_n\Delta z_n\\k_t\Delta z_t\end{bmatrix} \tag{4}$$

In the formula, F_n represents the normal contact force component, F_t represents the tangential contact force component, k_n represents the equivalent normal contact stiffness, k_t represents the equivalent tangential contact stiffness, Δz_n refers to the normal indentation of the tool relative to the surface of the plate, Δz_t is the tangential relative displacement between the tool and the plate, $\mathbf{F}_e$ and is the total contact force vector including the normal and tangential components.

Due to the elastoplastic behavior of the material, elastic recovery occurs during the unloading stage, leading to deviations in the molding profile. A simplified recovery model can be used to correlate the equivalent thickness recovery with the stress state:

$$\Delta h_r = \frac{\sigma_y - \sigma_r}{E} \tag{5}$$

In the formula, Δh_r is the equivalent elastic recovery in the thickness direction of the plate; σ_y is the yield stress of the material; σ_r is the residual stress after unloading; E and is the elastic modulus of the material.

2.3 Force-Position Cooperative Control Architecture Design

As shown in Figure 1, based on the aforementioned dynamics and contact model, this study constructs a collaborative control architecture coupling outer-loop force control and inner-loop pose control. The outer loop uses the normal forming force as the main control variable, and generates equivalent trajectory compensation based on force deviation.

$$\Delta x_f = K_f \left(F_d - F_n \right) \tag{6}$$

In the formula, Δx_f represents the normal displacement correction amount generated by the outer ring, K_f is the force feedback gain, which can be a scalar or a diagonal matrix, F_d is the desired normal forming force, F_n and is the actual normal contact force, the value of which can be obtained from formula (4). This compensation amount is superimposed on the reference trajectory to suppress force fluctuations caused by stiffness changes and local instability of the plate.

The inner loop achieves high-precision tracking of the corrected trajectory in the task space, employing a position-velocity-compensation hybrid control law:

$$\mathbf{u} = K_p \left(\mathbf{x}_d - \mathbf{x} \right) + K_v \left(\dot{\mathbf{x}}_d - \dot{\mathbf{x}} \right) + \Delta x_f \mathbf{e}_n \tag{7}$$

Where, $\mathbf{u}$ represents the control input in the task space, K_p and and K_v are the gain matrices for position and velocity, respectively, $\mathbf{x}_d$ and $\dot{\mathbf{x}}_d$ represents the desired pose and velocity, while $\mathbf{x}$ and $\dot{\mathbf{x}}$ correspond to the actual pose and velocity, $\mathbf{e}_n$ and is the unit vector in the tool normal direction. The closed-loop control of equations (1)-(3) is realized through inverse kinematics and inverse dynamics mapping.

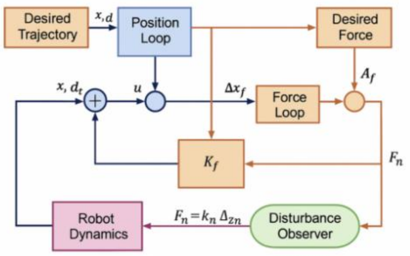

Fig. 1. Overall architecture diagram of force-position co-control

2.4 Force-Position Cooperative Control Architecture Design

Discrete implementation of the sampling period, computation, and sensing delays alters the closed-loop characteristics of the coordinated control. The stability analysis of the linearized state-space model can be expressed as follows:

$$K_f, K_p, K_v \tag{8}$$

Its characteristics are given by the closed-loop characteristic equation:

$$\det(\lambda I - (A - BK)) = 0 \tag{9}$$

Here, $\mathbf{x}_s$ is the linearized state vector, A represents the state matrix, B is the input matrix, is K the combined gain matrix synthesized I from the force loop and position loop gains, is the identity matrix, λ and are the closed-loop eigenvalues. By adjusting K_f, K_p, K_v parameters, all real parts can be λ made negative, thus balancing response speed with suppressing error oscillations and high-frequency amplification.

the system matrix A and B the sum of the values depend on the values of the robot dynamics parameters and the typical parameters of the material properties (see Table 1). These parameters are used to form the mass matrix, damping term, and contact stiffness, so as not to affect the distribution of closed-loop poles and error propagation velocity.

Table 1. Key parameters of robot dynamics and material properties of sheet metal

Parameter	Symbol	Value	Unit
Link equivalent inertia	–	12.4	kg·m^2
Joint viscous damping	–	0.32	N·m·s /rad
Normal contact stiffness	k_n	4.5× 10^4	N/mm
Tangential contact stiffness	k_t	1.2× 10^4	N/mm
Elastic modulus	E	68	GPa
Yield stress	σ_y	215	MPa
Sheet material density	–	2.7	g/cm^3

3 Error Modeling and Path Planning Optimization Method for Incremental Metal Forming

3.1 Decomposition of Molding Error Sources

Based on the dynamic model and force-position cooperative control structure in Chapter 2, s_k the progressive forming error of the robot is represented nodally according to the trajectory arc length. At the k node, the normal error of the plate surface is represented as e_k^n, the tangential error is represented as e_k^t, and the total error is regarded as the synthesis of three components: tool offset, plate springback, and force-position coupling disturbance.

Tool offset error originates from the robot's compliance and F_e the changes in joint clearance under load, and can be deduced from the end displacement using dynamic models (1) to (3). Springback error is related to contact and recovery models (4) and (5), and manifests as contour reduction during the unloading phase. Coupling disturbance error is caused by abrupt changes in contact stiffness, friction fluctuations, and control delays, leading to random shifts in pose and forming force. Therefore, the error state vector ek is defined as [insert error here] $\mathbf{e}_k = \left[e_k^n e_k^t \right]$, thus providing state variables for subsequent error observation and path improvement.

3.2 Online Compensation Model Based on Error Observability

Discrete implementationWithin the existing sensor configuration and force-position coordinated control framework, an observation equation is established for the error state of discrete nodes.

$$\mathbf{y}_k = C_e \mathbf{e}_k + \mathbf{v}_k \tag{10}$$

In the formula, $\mathbf{y}_k$ is the vector observed at the k-th node, which is obtained by integrating online profile measurement, end displacement, and contact force. $\mathbf{e}_k$ is the error state vector, which includes normal error e_k^n, tangential error e_k^t, and may also have local gradient components. C_e is the mapping matrix from error to observation, $\mathbf{v}_k$ and is the measurement noise vector.

That (A_e , C_e) is observable, a discrete error observer is introduced to predict and correct the error:

$$\hat{\mathbf{e}}_{k+1} = A_e\hat{\mathbf{e}}_k + B_e\mathbf{u}_k + L_e\left(\mathbf{y}_k - C_e\hat{\mathbf{e}}_k\right) \tag{11}$$

In the formula, $\hat{\mathbf{e}}_k$ represents k the error estimation vector of the i-th node, $\hat{\mathbf{e}}_{k+1}$ represents the error prediction vector of the next node, A_e represents the error state transition matrix, B_e represents the control input influence matrix, $\mathbf{u}_k$ represents the control input vector, which includes trajectory commands and force compensation, and L_e represents the observation gain matrix, which is tuned via pole setting or the minimum variance criterion. The observer output $\hat{\mathbf{e}}_k$ serves as the input to the compensation module in Figure 2, enabling real-time correction of the nominal path.

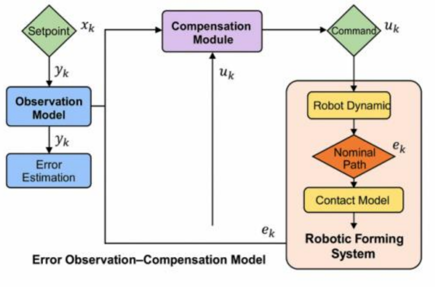

Fig. 2. Flowchart of the error observation-compensation model

3.3 Path Planning Optimization Strategy

After obtaining the error estimate $\hat{\mathbf{e}}_k$ and normal forming force $F_n\left(s_k\right)$, the nominal trajectory in Chapter 2 is replanned with accuracy guidance. First, $\partial F_n / \partial s$ a threshold is set based on the force gradient along the path γ_F , and $\left|\partial F_n / \partial s\right| > \gamma_F$ the section is segmented and the nodes are densified to give higher adjustment freedom to the high load variation area. Second, $\left|\hat{e}_k^n\right|$ the feed step size and step depth are adaptively adjusted according to the magnitude of the force gradient: a larger step size and pressure increment are used when the error is small and the force gradient is gentle, and the step size and step depth are reduced when the error is large or the force gradient is steep to suppress the amplification of force-position coupling disturbance.

The node error field is further interpolated in the plate coordinate system to generate a continuous error field, which drives the local path to be denser again and determines the direction of the normal compensation vector. Fig. 3 compares the tool trajectory and forming force distribution under the uniform step path, the segmented path based on the forming force gradient, and the denser path excited by the error field, providing a visual basis for subsequent algorithm solution and parameter tuning.

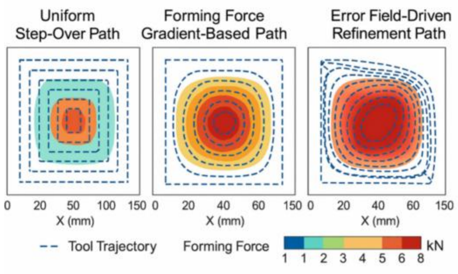

Fig. 3. Schematic diagram of tool trajectory and force distribution under different path planning strategies.

3.4 Optimization Algorithm Solution

Building upon the aforementioned error modeling and path structure, the position and normal compensation of each node are treated as improvement variables to form a multi-objective cost function. This reduces the mean square error of the contour and the fluctuation of the normal force, and forces are constrained by force limits, maximum step size/step depth, and kinematic reachability. Under the same hardware environment, using an Intel i7 processor and a control time of 2ms, 10 simulations were performed on the same target surface (a hyperbolic panel with dimensions of 100mm x 100mm) for each of the three path planning algorithms. Their average computational cost and convergence characteristics were obtained, and relevant information is shown in Table 2. It can be seen that by relying on the denser planning of the error field, the mean square error of the formed contour is significantly reduced with a slight increase in overall CPU time.

Table 2. Computational cost and convergence characteristics of different path planning algorithms

Algorithm	Avg. time per iteration / ms	Iterations to converge	Total CPU time / s	Final mean contour error / mm
Uniform step planning	1.8	120	0.22	0.46
Force-gradient segmented planning	2.3	95	0.22	0.31
Error-field refined planning	3.1	110	0.34	0.21

4 Experimental Platform Construction and Accuracy Optimization Results

4.1 Experimental Platform

To verify the force-position cooperative control and path planning methods presented in Chapters 2 and 3, this study created an incremental forming platform comprising a six-axis robot, a linear slide, and a control cabinet. The end effector assembles a forming head and integrates a six-dimensional force sensor and encoder to achieve high-precision pose measurement. The sheet metal is fixed using an adjustable stiffness fixture (as shown in Figure 4). The system adopts a force / position dual-loop structure. The host computer issues the trajectory and compensation values offline, while the real-time controller performs force signal acquisition and feedback adjustment. Six experimental conditions were designed based on curvature and forming depth; parameter configurations are detailed in Table 3.

Table 3. Experimental conditions of incremental sheet forming tests

Case ID	Sheet material	Thickness / mm	Step-over / mm	Target depth / mm	Path strategy
A1	AA5052	1.0	8	15	Uniform step-over
A2	AA5052	1.5	6	20	Uniform step-over
A3	AA6061	1.5	6	25	Force-gradient segmented
A4	AA6061	2.0	4	30	Force-gradient segmented
A5	DC01 steel	1.2	6	20	Error-field refined
A6	DC01 steel	1.5	4	30	Error-field refined + compensation

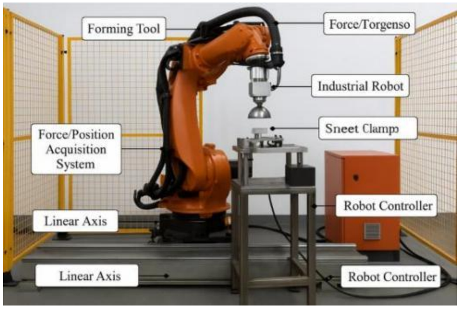

Fig. 4. Photo of the industrial robot progressive prototyping experimental platform

4.2 Performance Verification Experiment of Force-Position Coordinated Control

Based on the three working conditions A1, A3, and A5 in Table 3, compare the differences in force stability and trajectory accuracy between pure position control and force-position cooperative control. In the experiment, the nominal trajectory and shaping parameters remained unchanged; only the control algorithm was changed. Force and pose data were obtained by sampling at 1 kHz and interpolating using the controller. Fig. 5 shows that the cooperative control effectively suppressed force fluctuations and instantaneous overshoot during the initial loading and curvature abrupt change phases. Further calculations of mean square error, steady-state error, peak error, and settling time (Table 4) show that when the cooperative control is in the 1.0-1.2 kN range, it reduces force fluctuations and mean square position error by approximately 35% and 40%, respectively, while maintaining the settling time within 80 ms. Furthermore, observations revealed further convergence of the peak error, confirming the robustness analysis conclusions in Chapter 2.

Table 4. Control accuracy indices for different control strategies

Case ID	Control strategy	Nominal force / kN	RMS position error / mm	Steady-state error / mm	Max overshoot / %	RMS force fluctuation / N	Settling time / ms
C1	Position-only	1.0	0.42	0.19	18	125	120
C2	Position-only	1.2	0.47	0.23	twenty two	148	135
C3	Force-position cooperative	1.0	0.25	0.09	9	82	92
C4	Force-position cooperative	1.2	0.29	0.11	11	94	98
C5	Coop. + error observer	1.0	0.21	0.07	7	73	88
C6	Coop. + error observer	1.2	0.24	0.09	9	81	91

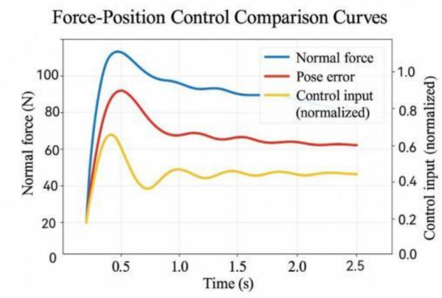

Fig. 5. Force-position control comparison curve

4.3 Experiment on the Effect of Path Planning Optimization

The path planning section selected five working conditions (A2-A6) from Table 3. Repeated forming operations were performed using three strategies: uniform step size, segmentation based on force gradient, and densification induced by the error field. After forming, point cloud data was obtained using structured light scanning, and then the point cloud was registered with the CAD surface to obtain the normal error. Figure 6 shows that the error is mostly concentrated in the high-curvature edge region and is significantly affected by the path strategy. To quantitatively compare the quality, the average value, maximum value, and surface roughness Ra of the statistical data were collected for both the planar and high-curvature regions. Then, a uniformity index was created based on the error variance. The final results are shown in Table 5. The error field promotes densification; in the high-curvature region, the average error decreased from 0.41 mm to 0.23 mm, and the uniformity index increased from 0.72 to 0.88, which is consistent with the force field and error distribution in Figures 3 and 6.

Table 5. Forming quality indices for different path strategies

Path strategy	Region	Mean error / mm	Max error / mm	Surface roughness Ra / μm	Uniformity index
Uniform step-over	Flat area	0.28	0.62	2.1	0.81
Uniform step-over	High-curvature	0.41	0.96	2.7	0.72
Force-gradient segmented	Flat area	0.22	0.55	2.0	0.84
Force-gradient segmented	High-curvature	0.31	0.79	2.4	0.80
Error-field refined	Flat area	0.19	0.47	1.9	0.87
Error-field refined	High-curvature	0.23	0.63	2.1	0.88

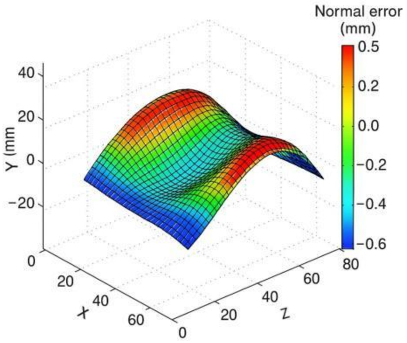

Fig. 6. Error distribution of the three-dimensional point cloud of the molding result

4.4 Verification under Different Materials and Thicknesses

To examine the suitability of the control-path collaborative method for varying materials and sheet thicknesses, three sheet materials—AA5052, AA6061, and DC01—with thicknesses ranging from 1.0 to 2.0 mm were selected. Forming operations were performed under the same surface curvature and control parameters. Compensation was then applied, followed by 3D scanning and CAD registration to statistically analyze the normal error. The maximum springback angle was also recorded to reflect the springback characteristics. Table 6 shows that the average error of the aluminum alloy sheet was reduced by approximately 40%, while the correction effect was more significant for the high-strength steel sheet, with the average error of 1.5 mm DC01 decreasing from 0.52 mm to 0.27 mm (a reduction of 48%). The results indicate that this method demonstrates good generalization and stability across different material systems.

Table 6. Forming error and compensation effects for different materials and thicknesses

Material	Thickness / mm	Mean error before / mm	Mean error after / mm	Error reduction / %	Max springback angle /°
AA5052	1.0	0.38	0.23	39	3.2
AA5052	1.5	0.35	0.21	40	2.8
AA6061	1.5	0.42	0.24	43	3.6
AA6061	2.0	0.44	0.26	41	3.9
DC01 steel	1.2	0.49	0.28	43	5.1
DC01 steel	1.5	0.52	0.27	48	5.6

5 Conclusions and Outlook

For robotic incremental metal forming relying on force-position cooperative control, accuracy issues exist. This study establishes a dynamic model that reflects contact stiffness and elastic recovery, and shapes a dual-loop cooperative control system, thus creating a comprehensive analysis system encompassing force-position coupling and closed-loop stability. Based on this, error observability analysis is used to form a nodal error observer, which is then integrated with force gradient segmentation and error field amplification paths to achieve adaptive updates of trajectory and normal compensation. Platform experiments show that this method can reduce trajectory mean square error, normal force fluctuation, and contour error in high curvature regions by approximately 40%, 35%, and 45%, respectively, while maintaining robustness and repeatability under various material and plate thickness conditions. This provides a generalizable technical approach for achieving high-precision, engineered robotic incremental forming.

Acknowledgement

This work was supported without any funding.

Conflicts of Interest

The authors declare no conflicts of interest.

References

1. Čabaravdić, M., Möllensiep, D., Kuhlenkötter, B., et al. (2024). Force-controlled path planning for robot-assisted incremental sheet metal forming: A new approach to addressing dimensional accuracy challenges. Precision Mechanics & Digital Fabrication, 1(4), 227-234.
2. Johra, M., Courteille, E., Deblaise, D., et al. (2022). Elasto-geometrical model-based control of industrial manipulators using force feedback: Application to incremental sheet forming. Robotics, 11(2), 48.
3. Kang, C., Jia, H., Zhao, E., et al. (2025). Development of an improved stiffness ellipsoid method for precise robot-positioner collaborative control in friction stir welding. Materials, 18(8), 1852.
4. Ye, X., Schwartz, M., & Hohmann, S. (2023). Enhancement of path tracking accuracy for physically coupled industrial robots by hybrid position-torque compensation. In 2023 European Control Conference (ECC) (pp. 1-8). IEEE.
5. To, X. D., Blanco, J. R., Zimmer-Chevret, S., et al. (2025). Robotized incremental sheet forming trajectory control using deep neural network for force/torque compensator and task-space error tracking controller. Mechatronics, 110, 103360.
6. Li, X., Yue, M., Wang, H., et al. (2025). Hierarchical constraint-based formation control strategy for multi-robot cooperative transportation system in warehouse using scenarios. Journal of Vibration and Control, 10775463251389027.
7. Han, S., & Zhao, R. (2025). Interior wall finishing design model incorporating motion redundancy optimization and active compliance control algorithm. Journal of Computational Methods in Sciences and Engineering, 14727978251366485.
8. Liu, J., Xu, D., & Guo, Y. (2024). Force control method for the variable robot payload in metal slag removal operation. In 2024 IEEE 13th Data Driven Control and Learning Systems Conference (DDCLS) (pp. 2070-2075). IEEE.
9. Bârsan, A., Popp, M. O., Rusu, G. P., et al. (2021). Robot-based incremental sheet forming - The tool path planning. In IOP Conference Series: Materials Science and Engineering (Vol. 1009, No. 1, p. 012004). IOP Publishing.
10. Racz, S. G., Crenganiș, M., Breaz, R. E., et al. (2022). Integrating trajectory planning with kinematic analysis and joint torques estimation for an industrial robot used in incremental forming operations. Machines, 10(7), 531.

Biographies

1. **Siwen Liu** Bachelor, Junior Engineer, working at Guangdong Beyho Technology Co., Ltd., with main research directions in artificial intelligence, robots, intelligent construction and production automation.

基於力-位協同控制的工業機器人在金屬漸進成型中的精度優化與路徑規劃

劉思文[1]

[1]广东毕要科技有限公司，佛山，中國，528000

摘要：工業機器人在漸進成形時存在精度不足、力波動較大以及路徑規劃缺少閉合環路等情況，針對這些問題,本研究提出一種力–位協同控制結合誤差驅動路徑改進的整合方法。首先建立動力學模型，該模型需包含接觸剛度與彈性恢復，以體現末端位姿與成形力間的耦合關係。而後依據誤差可觀測性構建離散觀測器，實現節點法向誤差的即時估計，並將估計結果與成形力梯度分段及誤差場加細相結合，得到自適應路徑規劃框架。六軸機器人平台實驗表明，該方法可使軌跡均方誤差降低約 40%，法向力波動減小約 35%，高曲率區域輪廓誤差削減約 45%，且在多材料、多板厚情境下仍能保持穩定的泛化性能，為機器人漸進成形的高精度、魯棒控制提供了可行的技術途徑。

關鍵詞：工业機器人；金属漸進形成；力–位協同控制；誤差觀測；路徑規劃優化

---

1. 劉思文，电气工程及其自动化专业學士，初級工程師，任職於广东毕要科技有限公司，主要研究方向為人工智能、机器人、智能建造和生產自动化。